Effect of the salt-induced micellar microstructure on the nonlinear shear flow behavior of ionic cetylpyridinium chloride surfactant solutions

D. Gaudino,[1,*] R. Pasquino,[1] H. Kriegs,[2] N. Szekely,[3] W. Pyckhout-Hintzen,[4] M. P. Lettinga,[2,5] and N. Grizzuti[1]

[1]*Dipartimento di Ingegneria Chimica, dei Materiali d della Produzione Industriale, Università degli Studi di Napoli Federico II, Piazzale Vincenzo Tecchio 80, 80125 Napoli, Italy*

[2]*Institute for Complex Systems, Forschungszentrum Jülich, 52425 Jülich, Germany*

[3]*Jülich Centre for Neutron Science Outstation at MLZ, Lichtenbergstrasse 1, 85747 Garching, Germany*

[4]*Jülich Centre for Neutron Science, Forschungszentrum Jülich GmbH, 52425 Jülich, Germany*

[5]*Laboratory for Soft Matter and Biophysics, KU Leuven, Celestijnenlaan 200D, 3001 Leuven, Belgium*

(Received 31 July 2016; revised manuscript received 5 December 2016; published 7 March 2017)

The shear flow dynamics of linear and branched wormlike micellar systems based on cetylpyridinium chloride and sodium salicylate in brine solution is investigated through rheometric and scattering techniques. In particular, the flow and the structural flow response are explored via velocimetry measurements and rheological and rheometric small-angle neutron scattering (SANS) experiments, respectively. Although all micellar solutions display a similar shear thinning behavior in the nonlinear regime, the experimental results show that shear banding sets in only when the micelle contour length $\bar{L}$ is sufficiently long, independent of the nature of the micellar connections (either linear or branched micelles). Using rheometric SANS, we observe that the shear banding systems both show very similar orientational ordering as a function of Weissenberg number, while the short branched micelles manifest an unexpected increase of ordering at very low Weissenberg numbers. This suggests the presence of an additional flow-induced relaxation process that is peculiar for branched systems.

DOI: 10.1103/PhysRevE.95.032603

I. INTRODUCTION

Wormlike micelles (WLMs) are one of the possible morphologies arising when surfactant molecules are dispersed in water. They are usually referred to as living polymers since they behave very similarly to covalently bonded polymer chains. The term "living" denotes the breaking and reforming character of the worms [1,2]. In the case of ionic surfactants, the addition of a penetrating (or binding) salt is responsible for the formation of the wormlike structure and, in some cases, for a morphological transition where linear worms are interconnected by sparse branched points. One well known example of such systems, used in the present work, is based on the surfactant cetylpyridinium chloride (CPC) and the binding salt sodium salicylate (NaSal). Many other similar systems have been studied in the literature and show the same quiescent microstructural features [3–10].

Flow strongly affects the dynamics of the micellar systems. In particular, flow-induced structures and instabilities can occur. Under steady shear flow conditions *linear* WLMs can show both shear thickening and shear thinning features, depending on the flow-induced micellar arrangement. Shear thickening is generally attributed to a fastening of the micelles, which become longer and give rise to a viscosity increase [11–14]. Shear thinning is indicative of an alignment of the micelles along the flow direction, which results in a decrease of viscosity as a function of the shear rate [15–20].

The flow-induced structures are often coupled to flow instabilities, such as gradient and vorticity shear banding [21]. Macroscopically, this phenomenon consists in a transition from a homogeneous to an inhomogeneous state characterized by a shear rate independence of the shear stress on the macroscopic shear rate [22,23]. Microscopically, shear banding is related to the coexistence of a paranematic band and a quasi-isotropic one, where micelles are aligned along the flow direction and entangled as in the quasi-quiescent state, respectively [19,24–26]. It must be stressed that, although shear banding has been widely observed, a definitive physical explanation, in particular of the microscopic mechanisms leading to shear banding development, is still missing.

Similar phenomena are observed in *branched* wormlike micellar systems. Shear thinning behavior has been found through both rheometric measurements and confirmed via scattering experiments [27–30]. However, at the same time, flow-induced turbidity and dichroism have been found to occur in micellar solutions containing a substantial number of branched micelles [31]. This has been proposed to be due to flow striation in microsized shear bands composed of highly branched, concentrated micellar solution coexisting with a nearly isotropic phase [9,10,32]. Nevertheless, as reported by Thareja *et al.* [29], no shear banding for such a system has been observed through velocimetry measurements.

The above literature analysis indicates that a clear and definitive understanding of the dynamics developed under shear flow is still missing both for linear wormlike micellar networks and, even more so, for branched WLMs. It must be pointed out that the great part of the micellar banding literature concentrates on specific samples, namely, those where the rheological and flow instabilities are more dramatic and pronounced. Conversely, the effect on the dynamical instabilities of the transition between different microstructures as obtained, for example, by tuning the binding salt concentration in ionic surfactant systems has received scarce attention.

In this work, a systematic study of the flow behavior of wormlike micelles of different microstructures, induced by a binding salt, is carried out. The aim is to identify the role of entanglements in the case of linear micelles and junction

*danila.gaudino@unina.it

points in the case of branched micelles on the relaxation mechanism. The contour length of both linear and the branched micelles has been identified as a crucial parameter for the onset of flow instabilities. To this end, rheometric small-angle neutron scattering (SANS) and heterodyne dynamic light scattering (HDLS) measurements have been performed on four micellar systems for which these parameters have previously been identified [8]. As will be discussed in the following sections, these techniques provide complementary information regarding the response of the micelles to the shear motion they have been subjected to. In particular, HDLS experiments, probing the flow profile of the complex fluids, highlight the predominant role of the contour length for the onset of flow instabilities and rheometric SANS tests, probing segment alignment, uncovered a possible additional relaxation mechanism, hidden to the rheological response, occurring only for micelles with junction points.

The paper is structured as follows. After this introduction, materials and methods are presented in the next section. The main results of rheological and scattering measurements are reported in Sec. III, which is followed by their discussion and comparison in Sec. IV. A summary is given and the relevant conclusions of the work are drawn in Sec. V.

II. MATERIALS AND METHODS

Micellar systems based on 100-mM CPC in 100-mM NaCl brine solutions have been studied at selected NaSal concentrations. NaCl is added to screen the long-range electrostatic repulsions among surfactant molecules [33,34], whereas NaSal is mainly responsible for the structural and dynamical changes of the system. Binding salt concentrations at 42.3, 60.9, 85.1, and 262 mM of NaSal have been prepared in order to obtain different morphological microstructures and, as a consequence, various linear dynamical responses [6,35]. As the amount of the sodium salicylate increases, micelles become elongated (42.3 mM), entangled linear (60.9 mM), and branched (85.1 and 262 mM) wormlike with different values of their contour length (shorter for the 85.1-mM solution) [35]. The linear viscoelasticity of the current analyzed systems has been recently studied [8].

All components have been obtained from Applichem Panreac and were used as received. Samples have been prepared by gently stirring the surfactant and the salts in deuterated water for a day at room temperature, followed by storage for at least two days in order to reach the equilibrium state. The deuterated water is required to increase the contrast needed to improve the quality of neutron scattering measurements.

All the experiments were conducted on the deuterated solutions in order to reduce possible extra differences and enable the comparison of results from the various techniques. Preliminary measurements have been performed also on protonated aqueous solutions, showing the same qualitative results displayed by the deuterated systems.

The steady-state dynamics of the solutions under shear flow have been studied through rheometric measurements. In particular, start-up experiments at different shear rates have been carried out on the systems. The steady values of both the shear viscosity and the shear stress were used to build up the flow curve for each sample. Experiments were carried out on a stress-controlled rheometer (AR G2, TA Instrument) equipped with a 60-mm, 0.017-rad cone-plate geometry. The temperature of 23 °C was controlled by a Peltier-lower-plate geometry. An antievaporation trap was used to minimize water evaporation and a delay time of 200 s after sample loading was applied before each experiment.

Heterodyne dynamic light scattering measurements have been performed on the selected surfactant micellar systems in order to investigate the velocity profiles developed under the shear flow. The homemade optical setup and the procedure to extract the data are described elsewhere [36]. Experiments were carried out by applying a constant angular velocity to the inner cylinder (43 mm in diameter) of a Couette geometry, characterized by a gap of 2.5 mm. The temperature was held constant at 23 °C by using a thermostatic bath. Velocity profiles were measured under steady-state conditions. Local shear rates can be calculated from the derivative of the flow profile (see, e.g., Fig. 3).

Small-angle neutron scattering measurements were carried out at the MLZ, Garching Research Centre (Münich, Germany) directing the beam along the radial direction and thus probing the shear-induced alignment of micellar segments in the flow-vorticity plane. Start-up experiments were performed *in situ* by using a stress-controlled rheometer (MCR 501, Anton Paar) with a Couette geometry (outer and inner cylinder diameters of 50 and 49 mm, respectively). The rheological results were compared with those obtained under off-beam conditions (see above). The excellent agreement between the two rheological measurements guarantees the reliability and consistency of the rheological and SANS measurements. A wavelength of 5 Å and a detector distance of 8 m ($5 \times 10^{-2} < q < 5 \times 10^{-1}$ nm^{-1}, with q the scattering vector) were set up during the rheometric SANS experiments at the constant temperature of 23 °C. Using standard procedures, the scattering intensities were corrected for transmission, an empty cell, and background scattering.

III. RESULTS

A. Rheology

The zero-shear rate viscosities of the selected surfactant solutions are reported in Fig. 1 as a function of NaSal [8]. Starting from the Cates model [4,37] and the works of Oelschlaeger *et al.* [35] and Gaudino *et al.* [6], the contour length for the selected micellar solutions (indicated by closed symbols in Fig. 1) is found to be roughly 270, 1800, 280, and 370 nm as the salinity is increased (see the Appendix for more details). Moreover, studies carried out on the same surfactant systems have revealed the formation and persistence of branched wormlike micelles in the saddle region of the zero-shear rate viscosity as a function of the salicylate [6,7,35]. Thus, from now on, we will refer to the different samples as their microstructures: linear short micelles (LSMs), linear long wormlike micelles (LLMs), branched short micelles (BSMs), and branched long wormlike micelles (BLMs). It should be pointed out that the above morphological evolution was recently confirmed by the molecular dynamics simulation study of Dhakal and Sureshkumar [38] on a very similar surfactant system (cetyltrimethylammonium chloride and NaSal). Molecular dynamics calculations confirm the

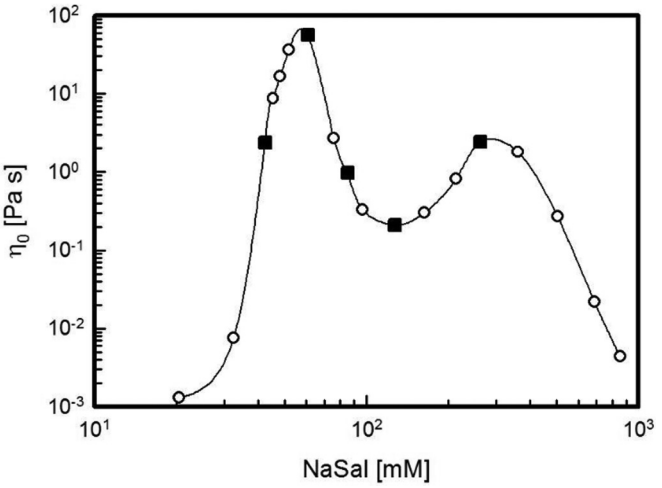

FIG. 1. Measured zero-shear rate viscosity (open circles) of the surfactant solutions as a function of [NaSal] (data adapted from [8]). Closed squares represent the four samples analyzed in this work.

presence of a significant number of branch points only in the NaSal concentration region between the two viscosity maxima. In particular, the simulations indicate that in the region of decreasing viscosity (left part of the saddle) a strong reduction of the micellar contour length is observed while short branches develop. The subsequent second increase in viscosity (right part of the saddle) is associated with the formation of a highly branched structure.

In Fig. 2 the shear viscosity η_s and the shear stress σ_s of the selected samples, as measured in the cone and plate geometry, are reported as a function of the engineered Weissenberg number Wi calculated as the product of the main relaxation time of the systems (the inverse of the crossover frequency between G' and G'') and the imposed shear rate. This choice allows for a direct comparison among systems having different dynamics depending on the salicylate content. Moreover, we refer to this number as the engineered Weissenberg number, as we impose a shear rate, while locally, in the gap of the cell, the shear rate may be different, as we will see later. Both η_s and σ_s have been normalized by the zero-shear-rate viscosity $\eta_{s,0}$ and the linear viscoelastic plateau modulus G_0. For more details, see the Appendix.

All solutions show a similar flow behavior, both in the linear and in the nonlinear regime. The turning point between the two regions (the Newtonian regime and the thinning regime) is always located at values of the Weissenberg number of about unity.

The linear regime displays a clear viscosity plateau; correspondingly, the steady shear stress increases linearly with a slope of one as Wi increases (on a log-log scale). The nonlinear regime is reached and the shear viscosity decreases as Wi overtakes unity. The slope of the shear stress curve approaches much smaller values in the nonlinear regime. The specific value of the slope in such a pseudoplateau stress region depends on the sample.

All flow curves show a second upturn at the highest values of Wi, with the exception of the BSMs. In this latter case, most probably, the upturn is not detectable due to instrument limitations, as the flow between the cone and plate becomes macroscopically unstable (due to edge fracture and consequent pouring out of the material).

The quantitative analysis of the flow curves has been carried out by assuming a power-law behavior [Eqs. (1) and (2)] [39], which fits the nonlinear data in the Wi range where the small slope of the flow curve is observed. In such a region, approximately spanning the range $2 < \mathrm{Wi} < 70$, the flow curve can indeed be described by a single flow index n with $R^2 \geqslant 0.99$:

$$\sigma_s \propto \dot{\gamma}^n, \tag{1}$$

$$\eta_s \propto \dot{\gamma}^{n-1}. \tag{2}$$

The fit results are summarized in Table I.

B. Velocimetry

The results of the HDLS measurements are shown in Fig. 3, where the velocity profiles at different Wi are reported as a function of the gap position x. The origin of the x coordinate

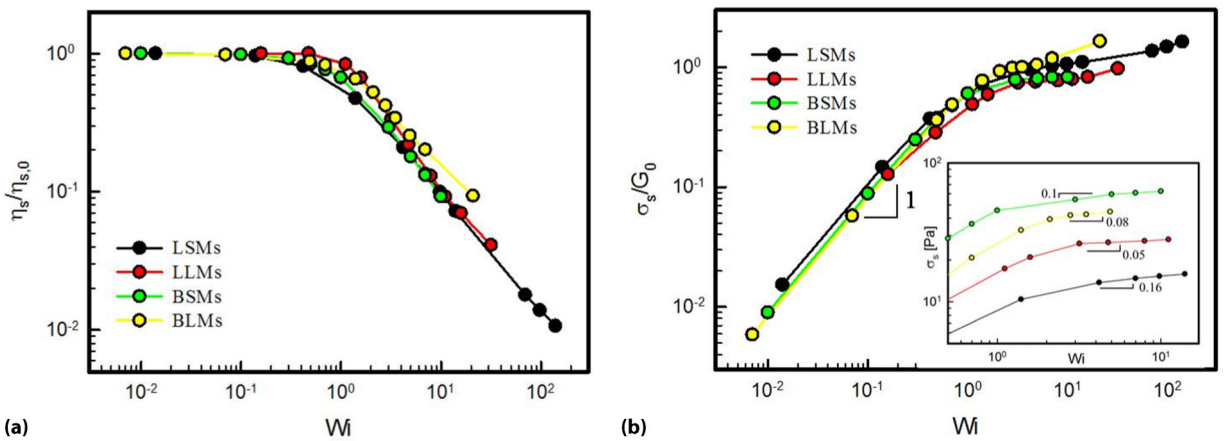

FIG. 2. Normalized (a) steady shear viscosity $\eta_s/\eta_{s,0}$ and (b) steady shear stress σ_s/G_0 as a function of Wi for the selected surfactant solutions (reported in legend). Here $\eta_{s,0}$ and G_0 are the zero-shear rate viscosity and elastic modulus plateau, respectively. The inset shows a zoomed in view of the steady shear stress σ_s in the pseudoplateau region.

TABLE I. Fit results of the index n of the selected surfactant solutions in a specific Wi range. Here τ is the main relaxation time obtained from the linear viscoelastic measurements (see the Appendix).

Samples	NaSal [mM]	τ [s]	n	Wi
LSMs	42.3	0.12	0.16	2–70
LLMs	60.9	1.5	0.05	2–20
BSMs	85.1	0.01	0.08	2–10
BLMs	262	0.06	0.1	2–5

coincides with the outer cylinder (radius R_2, not moving, $x = 0$). The maximum value of x corresponds to the wall of the inner cylinder (radius R_1, moving, $x = R_2–R_1$).

In the linear regime, the velocity profiles of all samples are not affected by the curvature of the Couette geometry. They also indicate the absence of slip at both cylindrical walls. In the nonlinear regime, different behaviors are observed. In particular, the velocity profiles of Figs. 3(a) and 3(c) are well described by a single smooth curve, whereas those of Fig. 3(b) are clearly composed of two straight lines of different slopes and therefore different shear rates. In this case, the corner point between the two lines moves towards the outer cylinder as the macroscopic shear rate increases. In Fig. 3(d) an intermediate behavior is displayed. Smooth velocity profiles are observed up to Wi values slightly larger than the onset of the nonlinear regime. For higher values of Wi (Wi $>$ 2.4), the profiles reproduce the double-slope response already seen for the LLMs [Fig. 3(b)]. Also in this case, the spatial region characterized by the higher shear rate becomes larger as the macroscopic shear rate increases.

The velocity profile in a Couette geometry, for a Newtonian fluid, can be fitted by solving the Navier-Stokes equation [40]

$$v(x) = \omega_0(R_2 - x)\left(\frac{(R_2 - x)^{-2} - R_2^{-2}}{R_1^{-2} - R_2^{-2}}\right), \qquad (3)$$

where ω_0 is the imposed angular velocity. In contrast, the velocity profile for a simple power-law fluid is represented by [40,41]

$$v(x) = \omega_0(R_2 - x)\left(\frac{(R_2 - x)^{-2/m} - R_2^{-2/m}}{R_1^{-2/m} - R_2^{-2/m}}\right), \qquad (4)$$

where m is the index of the power law. Obviously, for $m = 1$, Eq. (3) is recovered.

For smooth velocity profiles Eqs. (3) (for Wi $<$ 1) and (4) (for Wi $>$ 1) have been used to fit the experimental data. The fitting results obtained using Eq. (4) are summarized in Table II. In all cases, very high values of the coefficient of variation have been obtained ($R^2 > 0.99$). Obviously, the nonlinear power-law fit cannot be applied to the long linear wormlike micellar sample, where only the broken profiles are observed. In this case the velocity profiles are well fitted by two straight lines. The same situation is encountered for BLMs when Wi $>$ 2.4.

C. Rheometric SANS

Small-angle neutron scattering measurements have been performed on solutions subjected to shear flow. The neutron beam was directed along the gradient direction so that the vorticity-flow scattering plane was probed, whereas the probed length scale is that relative to segments of micelles [8]. In Fig. 4 the intensity two-dimensional (2D) patterns are presented as a function of Wi (x axis) and [NaSal] (y axis). As shown in Fig. 4, in the linear regime (Wi $<$ 1) all the 2D patterns are isotropic. As Wi increases, an anisotropic character arises for all the samples, though the quality and degree of alignment is sample dependent. In particular, BSMs display a pronounced elliptical scattering shape already at Wi $\cong$ 1, whereas the longer micellar solutions (LLMs and BLMs) are characterized by very similar 2D patterns, which assume a butterflylike shape at Wi $>$ 10. Only at much higher Wi (Wi $>$ 100), a weak butterfly shape arises also for the lowest salt concentration system.

To quantify the SANS information the azimuthal scattered intensity $I(q,\psi)$ along the projected azimuthal angle ψ has been fitted in order to obtain the scalar order parameter $\langle P_2(\psi)\rangle$ [42,43]. This is a good measure of alignment of the segments along the flow direction [44], but, as it represents only a projection of the orientational distribution on the vorticity-flow plane, is probably lower than the overall orientational order parameter. The results of the fit are summarized in Fig. 5, where $\langle P_2(\psi)\rangle$ is presented as a function of Wi for each sample.

The shear rate dependence of $\langle P_2(\psi)\rangle$ is distinctly different for the four samples. The increase of the orientational order parameter sets in when the nonlinear regime (Wi $>$ 1) is reached for all samples, with the exception of the BSMs. In this case, indeed, $\langle P_2(\psi)\rangle$ departs from zero already at Wi $\ll$ 1. This feature seems to be characteristic of branched short wormlike micelles. As clarified in the Appendix, the surfactant sample corresponding to the viscosity minimum in the viscosity vs NaSal concentration (Fig. 1) shows an increase in $\langle P_2(\psi)\rangle$ already in the limit of the linear regime (Wi $\ll$ 1). More details about the fit model and the $\langle P_2(\psi)\rangle$ dependence on the micellar microstructures are provided in the Appendix.

IV. DISCUSSION

The linear response of the micellar solutions has been found to strongly depend on their morphology, which is in turn controlled by the concentration of the binding salt [6,7,22,35]. Rheological steady-state measurements show the same qualitative response, although the microstructures of the various solutions are different [6,8,35]. All samples display a shear thinning behavior that can be described by a simple power-law expression characterized by a very small, or zero, power-law index (Fig. 2). This macroscopic approach, therefore, cannot distinguish between the microstructural diversities, thus calling for deeper investigations of the scale of the local flow, using heterodyne dynamic light scattering, as well as segment orientation of the micelles under shear flow, using rheometric small-angle neutron scattering. This combination allows us to investigate if there is a link between the microstructure and flow instabilities.

In the following, both the flow and the structural results presented in the preceding section are discussed in terms of the developing microstructures characterizing the sheared system.

Linear short micelles. The flow dynamics of the linear, slightly entangled micellar system is characterized by a

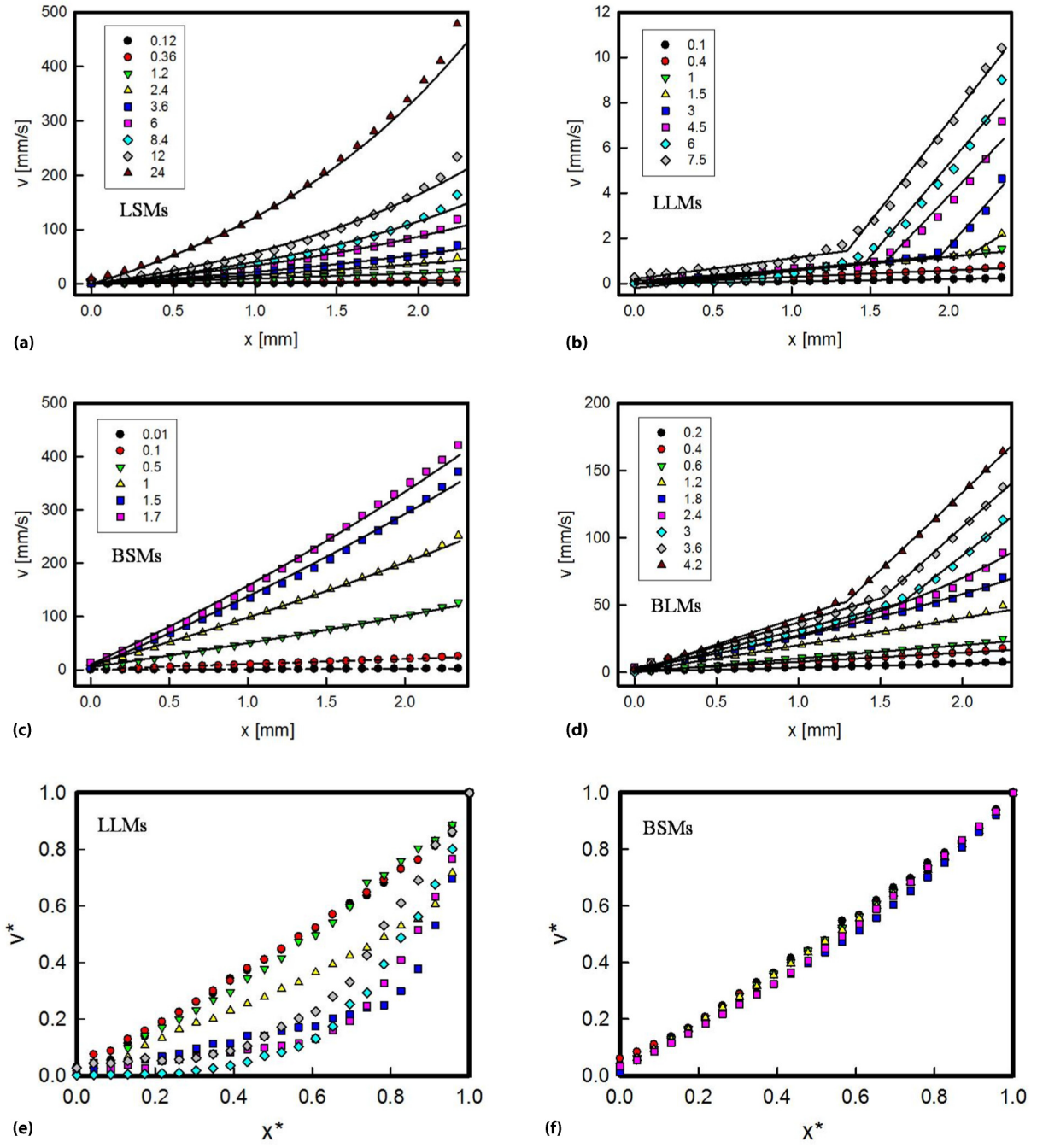

FIG. 3. Velocity profiles at different engineered Weissenberg numbers (see the legend and text for details) of (a) LSMs, (b) LLMs, (c) BSMs, and (d) BLMs. Fit curves are shown as solid black lines (see the text for details about the fit). Normalized velocity profiles are shown for (e) LLMs and (f) BSMs, with $v^* = v/v_0$ (v_0 is the velocity of the rotating cylinder) and $x^* = x/(R_2 - R_1)$. The legends for (e) and (f) are the same as in (b) and (c), respectively.

TABLE II. Fit results of the index m of the selected surfactant solutions.

Samples	NaSal [mM]	Shear banding	m
LSMs	42.3	no	0.15
LLMs	60.9	yes	
BSMs	85.1	no	0.38
BLMs	262	yes[a]	0.14

[a]With Wi > 2.4.

shear thinning behavior at Wi > 1 with a power-law index $n = 0.16$ (Fig. 2, Table I). The increasing alignment is accompanied by the alignment of the micelles along the flow direction for Wi > 1 as can be inferred from rheometric SANS experiments. As Wi further increases, the alignment becomes more pronounced and, consequently, the shear viscosity of the system decreases. However, the increase in alignment is very moderate as compared to the other systems (see Fig. 5). Moreover, the shear thinning behavior, which is of the same order as the other systems, does not lead to any shear banding

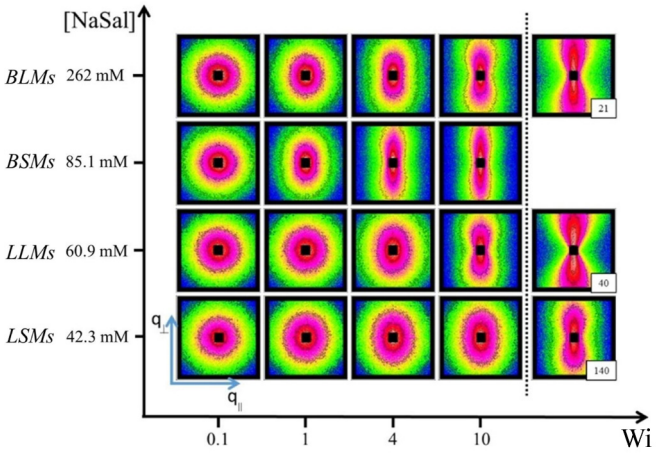

FIG. 4. SANS 2D patterns of the selected surfactant solutions as a function of the engineered Weissenberg number Wi. In the last column, the exact Wi values are specified.

phenomenon. Instead, the velocity profiles developed in the sheared sample become smoothly curved, once the nonlinear regime is established [Fig. 3(a)]. This behavior has been widely observed in literature [18,19,45,46] and is consistent with the macroscopic power-law response. In quantitative terms, the index n characterizing the power law of the macroscopic rheological data in the shear thinning region ($n = 0.16$) is in excellent agreement with the index m of Eq. (4) describing the velocity profiles developed in the nonlinear regime ($m = 0.15$).

Linear long micelles. In this case, the macroscopic response is coupled to the occurrence of the shear banding flow instability, although the rheological characteristics are the same as for the linear short micelles. As widely accepted in the literature [20,23–25], shear banding consists in the formation of two separated domains characterized by different values of the shear rate due to different micellar alignment. Our measured velocity profiles confirm previous experiments,

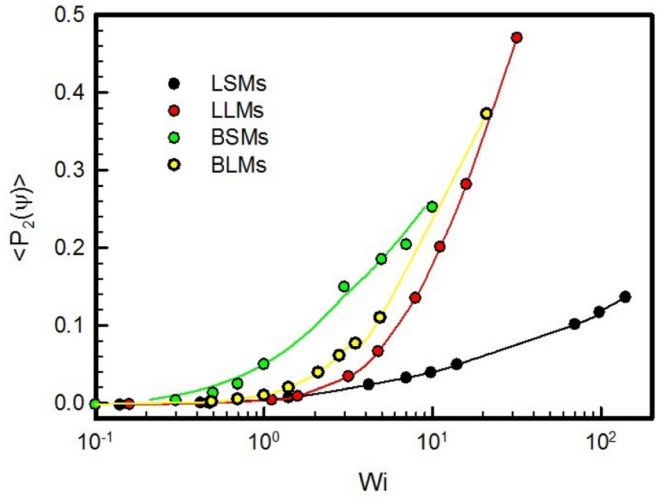

FIG. 5. Order parameter $\langle P_2(\psi)\rangle$ as a function of the engineered Weissenberg number Wi of the selected surfactant solutions (see the legend). The solid lines are guides for the eye.

indicating the two different domains of the sheared solution [Figs. 3(b) and 3(e)]. In particular, the local shear rate of the low shear rate band assumes a value [$\mathrm{Wi_{low}} = 1.5$ from HDLS, Fig. 3(b)] that is at the onset of the shear stress plateau. In addition, velocimetry results allow us to quantitatively monitor the growth of the high shear band, whose width is identified by the position of the corner point (corner between the two bands; see Fig. 3). The normalized width δ^* has been calculated as

$$\delta^* = 1 - \frac{x'}{R_2 - R_1}, \tag{5}$$

where x' represents the position in the gap at which the interface between the two bands occurs. In Fig. 6, δ^* and the local Wi ($\mathrm{Wi_{low}}$ and $\mathrm{Wi_{high}}$ for the low and the high shear bands, respectively) are plotted as a function of engineered Weissenberg number Wi. More details on the determination of both δ^* and local values of Wi are available in the Appendix.

Recent scanning narrow-aperture flow ultrasmall-angle neutron scattering experiments have demonstrated that the formation of shear bands is connected to the strong alignment of micelles at the rotating wall, where they align along the flow direction and form a high shear rate band, whereas the remaining region is composed of less ordered micelles, constituting the lower shear rate band [10,26,46]. This is exemplified by butterflylike patterns as observed earlier by Refs. [10,31,47–49]. Our rheometric SANS experiments agree with this behavior. Note that, in our case, the scattering experiments performed on the sheared solutions provide averaged information on the structure developed in the flow-velocity gradient plane. Hence, the 2D patterns are a superposition of the local information along the velocity gradient direction. As a consequence, when the sheared sample splits into two bands, two qualitatively different patterns overlap: one, strongly elliptical, associated with the highly sheared band, the other, essentially isotropic, representative of the less aligned segments. Thus, the increase in the orientational ordering thus corresponds to the increasing contribution of the high shear rate band.

Branched short micelles. Branched short micelles display some interesting peculiarities. First of all, a scattering anisotropy can be detected already at $\mathrm{Wi} \ll 1$. Moreover, in the nonlinear regime, the shear thinning character finds its SANS counterpart in simply elliptical scattering patterns. Correspondingly, the velocity profiles appear to be smoothly curved. This is surprising as the system is strongly shear thinning, as confirmed by the rheological measurements ($n = 0.08$). Indeed, the index of the power law considered to fit the curved velocity profiles is very high ($m = 0.38$), which confirms the less pronounced nonlinear feature characterizing the flow field of the branched short micellar system at $\mathrm{Wi} > 1$. This is clearly shown in Fig. 3(f), where the normalized velocity profiles only slightly differ from the linear ones. Thus, in this case the alignment is representative for the full sample, as there is no averaging of shear banded regions and there is clearly a different shear thinning mechanism at hand.

Branched long micelles. The branched long micellar system exhibits an intermediate behavior between those of linear long and branched short WMLs, previously discussed. On the one hand, like BSMs, the 2D patterns show anisotropy for Wi=1 and the clear nonlinear velocity profiles are observable at $\mathrm{Wi} = 2.4$. On the other hand, as in the case of LLMs, the

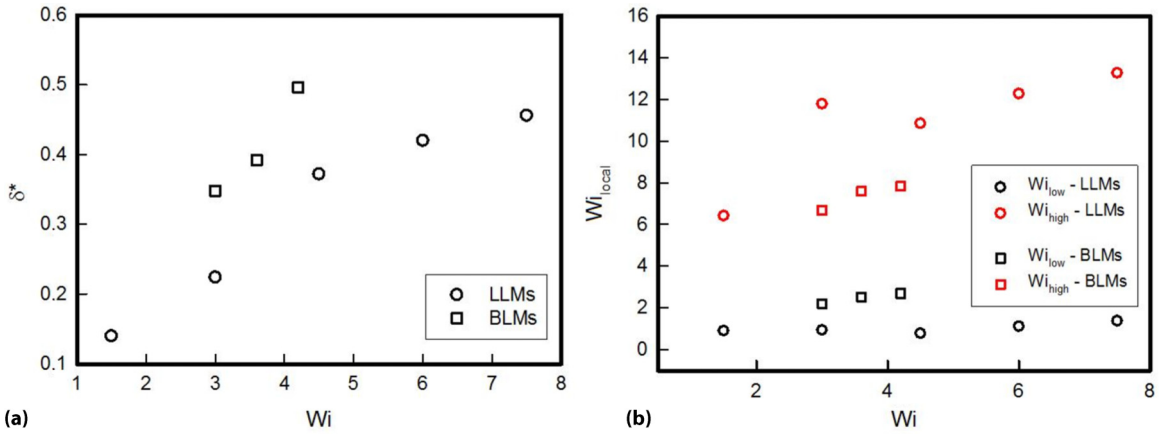

FIG. 6. (a) Normalized width δ^* of the high shear band as a function of the engineered Weissenberg number Wi for the LLMs and BLMs and (b) local Weissenberg number $\mathrm{Wi}_{\mathrm{local}}$ of the low shear band $\mathrm{Wi}_{\mathrm{low}}$ and the high shear band $\mathrm{Wi}_{\mathrm{high}}$ as a function of the engineered Weissenberg number Wi for the LLMs and BLMs (see the legend).

disagreement between the two power-law exponents employed to independently fit the rheometric and the HDLS experimental data is found again ($n = 0.1$ and $m = 0.14$, respectively). Note that, for BLMs, the difference between n and m seems to be less pronounced than the similar discrepancy previously observed for the LLMs. This result has to be ascribed to the occurrence of the shear banding instability at $\mathrm{Wi} > 2.4$, which does not allow us to fully investigate the nonlinear flow field. For higher Weissenberg numbers, indeed, the velocity profiles are again composed of two straight lines [whose characteristic shear rates fall again in the $\dot{\gamma}$ region where the shear stress plateau occurs, namely, at $\mathrm{Wi}_{\mathrm{low}} = 3$ from HDLS, Fig. 3(d)] and 2D butterflylike patterns arise. As for the case of the linear long WLMS, the growth of the high shear band and the local Weissenberg numbers are presented in Fig. 6.

The direct comparison between δ^* of the LLMs and BLMs clearly shows that the bands are broader for BLMs as compared to LLMs at fixed Wi.

The most general result of this analysis regards the possibility of producing samples that have nearly identical macroscopic shear thinning behavior but completely different local flow behavior: Branched short micelles do not show shear banding, while long linear ones display a marked flow instability. This strongly hints at the fact that a prerequisite for shear bands to form is not only the global shear thinning behavior, but also their microstructure. Here it seems that a crucial role is played by the contour length, as only long linear and branched micellar solutions, with a sufficiently high $\bar{L}$ of roughly 1800 and 370 nm, respectively [6,35], display the shear banding phenomenon. Hence, the longer the contour length, the easier the occurrence of flow instability, independently of the details of the micellar network (entangled or branched).

This does not mean that branching is irrelevant for the flow behavior. On the contrary, the short branched systems display surprisingly high alignment at very low Weissenberg numbers (see the Appendix for more details). This could be due to an additional relaxation mechanism, which can be ascribed to the presence of branched points [6,48].

This might also explain the small difference between both systems with long WLMs that form shear bands as soon as the nonlinear regime is reached.

V. CONCLUSION

In this work the influence of the microstructure of wormlike micelles on its flow response was studied, using different levels of binding salt to produce short and long, linear and branched wormlike micelles.

Shear thinning is always observed, with a thinning intensity that is almost independent of the contour length value and the nature of the micellar connections (entanglements or branch points).

Hence, the macroscopic behavior describing such dynamics is almost identical for these four systems.

On the contrary, spatially resolved measurements of the flow field developed along the velocity gradient direction show very different behaviors. In the case of short and long linear micelles, the average flow behavior characterizing linear WLMs, obtained from the HDLS measurements, corresponds to the prediction from the power-law fitting of the shear thinning region, while shear banding instability is observed for those systems characterized by linear and branched *long* micelles. Hence, while the micellar contour length value seems to enhance flow instabilities, the nature of the micellar connections seems to be irrelevant as well as the degree of the macroscopic shear thinning.

In addition to this different flow behavior, we also observe important structural differences between the systems in the degree of ordering as a function of shear rate, as clarified in Fig. 5, where the order parameter $\langle P_2(\psi)\rangle$ is plotted as a function of the engineered Weissenberg number Wi. Surprisingly, for the branched micelles $\langle P_2(\psi)\rangle$ is nonzero already at $\mathrm{Wi} < 1$ (as suggested also by the anisotropy shown in Fig. 4), while for the other systems it departs from zero at $\mathrm{Wi} > 1$.

However, it must be pointed out that we define our Weissenberg number as the product between the engineered shear rate and the main relaxation time obtained from the linear mechanical spectrum of the system. The departure from 0 of $\langle P_2(\psi)\rangle$ for Weissenberg numbers much smaller than 1 suggests the existence of an additional characteristic time, not visible in the rheological response. This additional relaxation process cannot be identified by the classical relaxation time given by the Cates theory (the geometrical mean between the

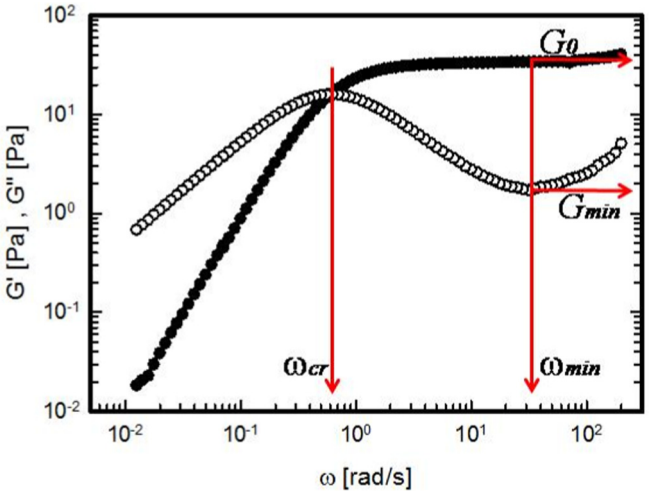

FIG. 7. Elastic (closed circles) and viscous (open circles) moduli as a function of the angular frequency ω for the surfactant micellar system at [NaSal] = 60.9 mM.

reptation time and the breaking time). Hence, for this system we assume the occurrence of a microstructural rearrangement of the branched micelles, which does not appear in the global rheological flow curve but is evidenced by scattering measurements.

Our observations open up many issues regarding the determination of the threshold value between the linear and nonlinear regimes. This finding is in line with many examples of complex systems, where such additional stress relaxation mechanisms cannot be detected through simple rheology. Examples include blends of architecturally different polymers with strongly disperse times [50–53]. In these systems, depending on the concentration of the various structures, the hierarchical relaxation mechanism of the different characters could be hidden in a rheological measurement, while showing up clearly in scattering experiments.

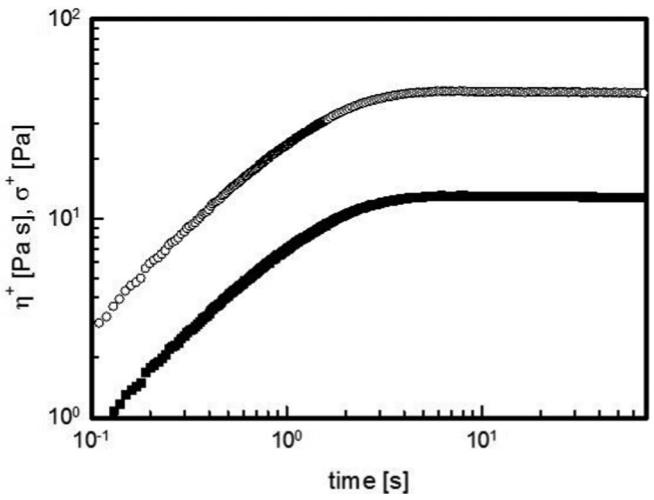

FIG. 8. Transient behavior of the shear viscosity (open circles) η^+ and the shear stress (closed squares) σ^+ at 0.3 s^{-1} for the surfactant micellar system at [NaSal] = 60.9 mM.

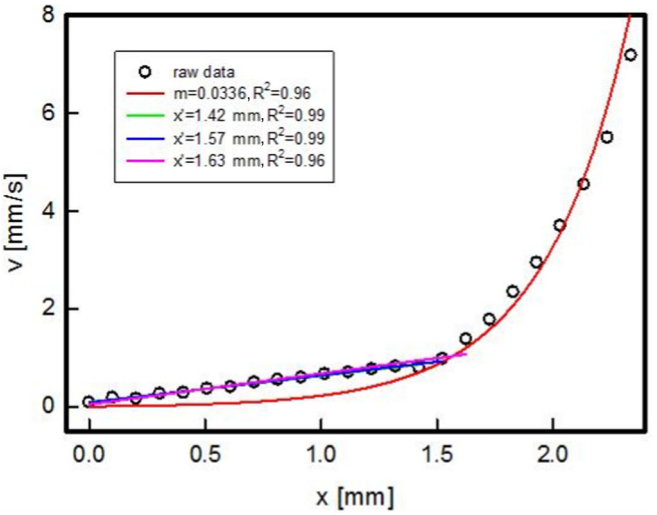

FIG. 9. Velocity profile of long linear WLMs ([NaSal] = 60.9 mM) at a shear rate of 3 s^{-1} (Wi = 4.5).

ACKNOWLEDGMENTS

The authors are grateful to Professor Francesco Greco for helpful comments and discussions. D.G. thanks the University of Naples Federico II for a fellowship program (Coinor-Programma Star) and the Jülich Forschungszentrum for financial and scientific support.

APPENDIX

1. Rheology

In this section some information regarding the rheological characterization of the micellar solutions is provided. To give an example of the procedure used to extract information from the linear viscoelasticity, in Fig. 7 the mechanical spectrum of

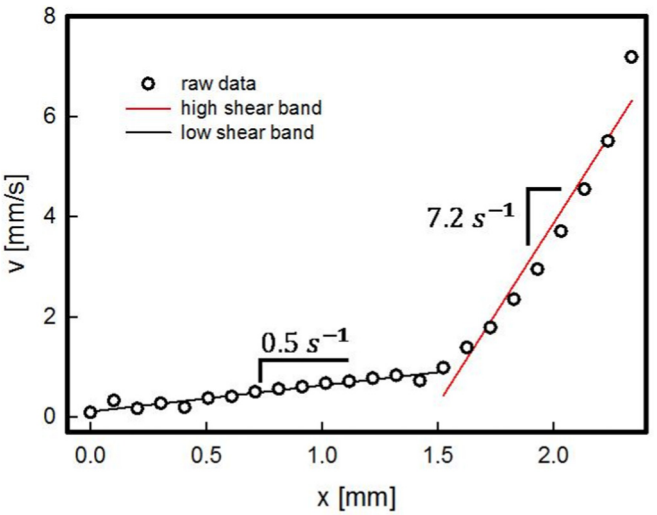

FIG. 10. Linear regressions of the velocity profile of long linear WLMs ([NaSal] = 60.9 mM) at a shear rate of 3 s^{-1} (Wi = 4.5). The red and the black lines represent the linear fit of velocity profile of the high and low shear bands, respectively. The slopes of the fits provide the local values of the shear rate.

TABLE III. Results of the fit procedure to determine and verify the width of the high shear band x' [normalized in δ^* following Eq. (5)] and to calculate the local Weissenberg numbers for the long linear WLMs ([NaSal] = 60.9 mM) at a shear rate of $3\,s^{-1}$ (Wi = 4.5).

$\dot{\gamma}_{low}$ (s^{-1})	$\dot{\gamma}_{high}$ (s^{-1})	Wi_{low}	Wi_{high}	$\overline{\delta^*}$	δ^*
0.5	7.2	0.75	10.8	0.37	0.37

LLMs is shown and the main rheological parameters, such as the crossover frequency ω_{cr}, the frequency corresponding to the minimum of G'', ω_{min}, and the elastic modulus plateau G_0 are indicated. From Fig. 7, the main relaxation time τ is obtained as the inverse of the crossover frequency, whereas the elastic modulus plateau G_0 can be directly taken from the mechanical spectrum, in correspondence with ω_{min}, i.e., the frequency where the loss modulus attains its relative minimum.

When all the parameters are available from the rheology, it is possible to estimate the contour length $\bar{L}$ of the micelles [37,54]

$$G_0 = \frac{k_B T}{\xi^3} \cong \frac{k_B T}{l_e^{9/5} l_p^{6/5}}, \tag{A1}$$

$$\frac{l_e}{\bar{L}} = \frac{G''_{min}}{G_0}, \tag{A2}$$

where l_e is the average length between two entanglement points, k_B is the Boltzmann constant, and T is the temperature. An average persistence length l_p of 20 nm has been assumed [55]. On the other hand, if the breaking and reforming time is not directly observable, estimation of $\bar{L}$ can be obtained following Gaudino *et al.* [6].

The shear viscosity and the shear stress have been measured through start-up experiments, which have been carried out on micellar solutions at different shear rates. The steady-state value (at long times) was then considered to build up the flow curve. An example is given in Fig. 8, where a start-up measurement at $0.3\,s^{-1}$ is reported for the LLMs.

2. Velocimetry

In this section additional information on the procedure used to fit the velocity profiles in the shear banding regime is provided. Equation (4) has been used to fit the flow field of long WLMs and it shows clear disagreement between the raw data and the predictions of the model under instability conditions. On the contrary, two straight lines nicely interpolate the velocity profiles in the shear banding regime, as expected for such systems [19,20]. Thus, we carefully checked the threshold between these two lines, considering the coefficient of determination as $R^2 \geqslant 0.99$.

An example of this procedure is given in Fig. 9, where the velocity profile of the long linear wormlike micellar system, at Wi = 4.5, is shown along with different fit attempts. In particular, the red solid line represents the velocity profile predicted by Eq. (4); green, blue, and pink solid lines are linear fits of the low shear band, considering the corner point x' at 1.42, 1.57, and 1.63 mm from the origin of the axis, respectively. In this case, $x' = 1.57$ mm since, as soon as a wider band is considered, R^2 decreases. Once the width x' is determined, the local Weissenberg number for the low and the high shear bands (Wi_{low} and Wi_{high}, respectively) can be calculated as the product of the relaxation time of the system and the slope of the related bands.

Working on the same system as in Fig. 9, an example of the above-mentioned procedure is given in Fig. 10. Here Wi_{low} and Wi_{high} are obtained as the product between the relaxation time of the system and the shear rate of the low and the high shear bands, respectively. Once the local Weissenberg numbers are determined, it is possible to verify the value of the normalized width of the high shear band as [20]

$$\overline{\delta^*} = \frac{Wi - Wi_{low}}{Wi_{high} - Wi_{low}}. \tag{A3}$$

The results calculated for the system taken as an example are provided in Table III.

3. Rheometric scattering

In this section additional information on the model used to fit the rheometric SANS data is provided. Figure 11(a) shows

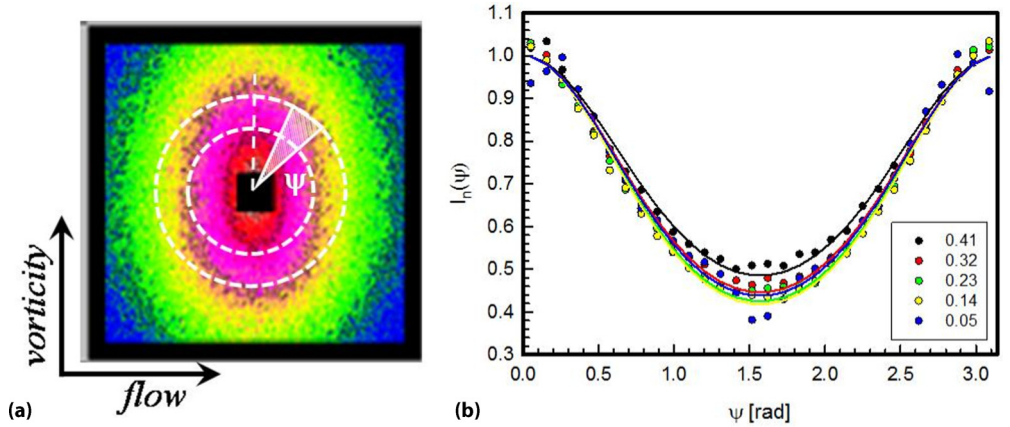

FIG. 11. (a) Example of the small-angle neutron scattering 2D pattern for LSMs under shear conditions ($\dot{\gamma} = 100\ s^{-1}$). The dashed lines indicate the q range where a q^{-1} dependence is typically found. (b) Normalized azimuthal intensity $I_n(\psi)$ as a function of ψ at different q values (in nm^{-1} in the legend) with relative fits (colored lines). The fits are shown to be insensitive to the different q selected.

a typical scattering pattern for LSMs under shear conditions and the shear-induced anisotropy is clearly displayed. In Fig. 11(b) the normalized azimuthal intensity profile $I_n(\psi)$ corresponding to the $I(q)$ range proportional to q^{-1} [area of the annulus in Fig. 11(a)] is shown as a function of ψ, the project azimuthal angle on the flow-vorticity plane, and can be fitted by [42]

$$I(q,\psi) \propto \exp[\alpha P_2(\psi) - 1], \tag{A4}$$

where α represents the width of the intensity profile and P_2 is the second-order Legendre polynomial. The scalar order parameter $\langle P_2(\psi)\rangle$ can be then calculated as [43]

$$\langle P_2(\psi)\rangle = \frac{\int_0^{\pi} \exp\{\alpha P_2(\psi)\} P_2(\psi) \sin(\psi) d(\psi)}{\int_0^{\pi} \exp\{\alpha P_2(\psi)\} \sin(\psi) d(\psi)} \tag{A5}$$

for rods and normalized azimuthal intensity $I_n(\psi)$ as a function of ψ at different q values (in nm^{-1} in the legend) with relative fits (colored lines). The fits are shown to be insensitive to the different selected q.

In this section, results related to an additional solution (at [NaSal] = 127 mM) are shown together with all the samples investigated in the main text. The relevance of this sample deals with the fact that it corresponds to the viscosity minimum in the viscosity vs NaSal concentration (Fig. 1). Thus, it provides crucial indications in the understanding of the alignment of the different micellar microstructures under shear flow, since it is composed of branched very short wormlike micelles (BVSMs). This system was not discussed in the main text because its nonlinear threshold is too high and could not be reached either by rheological or by velocimetry measurements. For this reason, only SANS data are available.

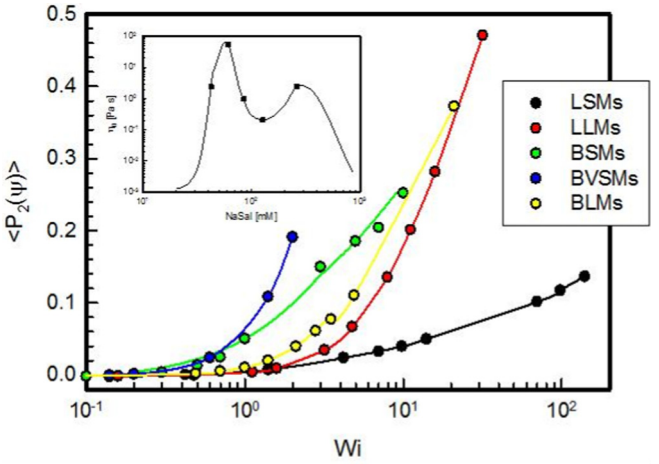

FIG. 12. Order parameter $\langle P_2(\psi)\rangle$ as a function of Wi of the selected surfactant solutions (see the legend). The solid lines are guides for the eye. The inset shows the samples along the viscosity curve.

Figure 12 shows the fitted parameter $\langle P_2(\psi)\rangle$ corresponding to all five samples. Confirming the generic trend of the fitted order parameter, at a fixed Wi, $\langle P_2(\psi)\rangle$ is the highest possible for the shortest branched micelles.

[1] M. E. Cates, Macromolecules **20**, 2289 (1987).
[2] U. Olsson, J. Börjesson, R. Angelico, A. Ceglie, and G. Palazzo, Soft Matter **6**, 1769 (2010).
[3] R. Angelico, S. Amin, M. Monduzzi, S. Murgia, U. Olsson, and G. Palazzo, Soft Matter **8**, 10941 (2012).
[4] M. E. Cates and S. J. Candau, J. Phys.: Condens. Matter **2**, 6869 (1990).
[5] C. A. Dreiss, Soft Matter **3**, 956 (2007).
[6] D. Gaudino, R. Pasquino, and N. Grizzuti, J. Rheol. **59**, 1363 (2015).
[7] S. A. Rogers, M. A. Calabrese, and N. J. Wagner, Curr. Opin. Colloid Interface Sci. **19**, 530 (2014).
[8] D. Gaudino, R. Pasquino, J. Stellbrink, N. Szekely, M. Krutyeva, A. Radulescu, W. Pyckhout-Hintzen, and N. Grizzuti, Phys. Chem. Chem. Phys. **19**, 782 (2017).
[9] M. A. Calabrese, S. A. Rogers, R. P. Murphy, and N. J. Wagner, J. Rheol. **59**, 1299 (2015).
[10] M. A. Calabrese, S. A. Rogers, L. Porcar, and N. J. Wagner, J. Rheol. **60**, 1001 (2016).
[11] W. Richtering, Curr. Opin. Colloid Interface Sci. **6**, 446 (2001).
[12] J. F. Berret, R. Gamez-Corrales, Y. Séréro, F. Molino, and P. Lindner, Europhys. Lett. **54**, 605 (2001).
[13] S. L. Keller, P. Boltenhagen, D. J. Pine, and J. A. Zasadzinski, Phys. Rev. Lett. **80**, 2725 (1998).
[14] B. M. Marín-Santibáñez, J. Pérez-González, L. De Vargas, F. Rodríguez-González, and G. Huelsz, Langmuir **22**, 4015 (2006).
[15] S. Förster, M. Konrad, and P. Lindner, Phys. Rev. Lett. **94**, 017803 (2005).
[16] V. Croce, T. Cosgrove, C. A. Dreiss, S. King, G. Maitland, and T. Hughes, Langmuir **21**, 6762 (2005).
[17] J. B. Hayter and J. Penfold, J. Phys. Chem. **88**, 4589 (1984).
[18] Y. T. Hu, C. Palla, and A. Lips, J. Rheol. **52**, 379 (2008).
[19] J.-B. Salmon, A. Colin, S. Manneville, and F. Molino, Phys. Rev. Lett. **90**, 228303 (2003).
[20] S. Manneville, Rheol. Acta **47**, 301 (2008).
[21] J. K. G. Dhont and W. J. Briels, Rheol. Acta **47**, 257 (2008).
[22] H. Rehage and H. Hoffmann, J. Phys. Chem. **92**, 4712 (1988).
[23] H. Rehage and H. Hoffmann, Mol. Phys. **74**, 933 (1991).
[24] N. A. Spenley, M. E. Cates, and T. C. B. McLeish, Phys. Rev. Lett. **71**, 939 (1993).
[25] J.-F. Berret, Langmuir **13**, 2227 (1997).
[26] A. K. Gurnon, C. Lopez-Barron, M. J. Wasbrough, L. Porcar, and N. J. Wagner, ACS Macro Lett. **3**, 276 (2014).
[27] B. A. Schubert, E. W. Kaler, and N. J. Wagner, Langmuir **19**, 4079 (2003).
[28] M. W. Liberatore, F. Nettesheim, N. J. Wagner, and L. Porcar, Phys. Rev. E **73**, 020504 (2006).
[29] P. Thareja, I. H. Hoffmann, M. W. Liberatore, M. E. Helgeson, Y. T. Hu, M. Gradzielski, and N. J. Wagner, J. Rheol. **55**, 1375 (2011).
[30] V. Herle, J. Kohlbrecher, B. Pfister, P. Fischer, and E. J. Windhab, Phys. Rev. Lett. **99**, 158302 (2007).
[31] B. A. Schubert, N. J. Wagner, E. W. Kaler, and S. R. Raghavan, Langmuir **20**, 3564 (2004).
[32] M. A. Fardin, L. Casanellas, B. Saint-Michel, S. Manneville, and S. Lerouge, J. Rheol. **60**, 917 (2016).

[33] G. Porte, R. Gomati, O. El Haitamy, J. Appell, and J. Marignan, J. Phys. Chem. **90**, 5746 (1986).
[34] S. J. Haward and G. H. McKinley, Phys. Rev. E **85**, 031502 (2012).
[35] C. Oelschlaeger, M. Schopferer, F. Scheffold, and N. Willenbacher, Langmuir **25**, 716 (2009).
[36] J. Delgado, H. Kriegs, and C. Rolando, J. Phys. Chem. B **113**, 15485 (2009).
[37] R. Granek and M. E. Cates, J. Chem. Phys. **96**, 4758 (1992).
[38] S. Dhakal and R. Sureshkumar, J. Chem. Phys. **143**, 024905 (2015).
[39] H. A. Barnes, J. F. Hutton, and K. Walters, *An Introduction to Rheology* (Elsevier, Amsterdam, 1989), Vol. 3.
[40] K. H. De Haas, D. Van Den Ende, C. Blom, E. G. Altena, G. J. Beukema, and J. Mellema, Rev. Sci. Instrum. **69**, 1391 (1998).
[41] C. W. Macosko, *Rheology: Principles, Measurements, and Applications* (Wiley-VCH, New York, 1994); R. G. Larson, *The Structure and Rheology of Complex Fluids* (Oxford University Press, New York, 1998).
[42] S. J. Picken, J. Aerts, R. Visser, and M. G. Northolt, Macromolecules **23**, 3849 (1990).
[43] B. Lonetti, J. Kohlbrecher, L. Willner, J. K. G. Dhont, and M. P. Lettinga, J. Phys.: Condens. Matter **20**, 404207 (2008).
[44] B. Hammouda, *Probing Nanascale Structures—The SANS Toolbox* (NIST, Gaithersburg, 2008).
[45] M. W. Liberatore, F. Nettesheim, P. A. Vasquez, M. E. Helgeson, N. J. Wagner, E. W. Kaler, L. P. Cook, L. Porcar, and Y. T. Hu, J. Rheol. **53**, 441 (2009).
[46] M. E. Helgeson, M. D. Reichert, Y. T. Hu, and N. J. Wagner, Soft Matter **5**, 3858 (2009).
[47] J. P. Decruppe, S. Lerouge, and J. F. Berret, Phys. Rev. E **63**, 022501 (2001).
[48] J. F. Berret, D. C. Roux, G. Porte, and P. Lindner, Europhys. Lett. **25**, 521 (1994).
[49] C. R. López-Barrón, A. K. Gurnon, A. P. Eberle, L. Porcar, and N. J. Wagner, Phys. Rev. E **89**, 042301 (2014).
[50] F. Lequeux, Europhys. Lett. **19**, 675 (1992).
[51] N. Ruocco, L. Dahbi, P. Driva, N. Hadjichristidis, J. Allgaier, A. Radulescu, M. Sharp, P. Lindner, E. Straube, W. Pyckhout-Hintzen, and D. Richter, Macromolecules **46**, 9122 (2013).
[52] K. Nakamura and T. Shikata, J. Phys. Chem. B **111**, 12411 (2007).
[53] T. C. B. McLeish, J. Allgaier, D. K. Bick, G. Bishko, P. Biswas, R. Blackwell, B. Blottière, N. Clarke, B. Gibbs, D. J. Groves, A. Hakiki, R. K. Heenan, J. M. Johnson, R. Kant, D. J. Read, and R. N. Young, Macromolecules **32**, 6734 (1999).
[54] R. G. Larson, J. Rheol. **56**, 1363 (2012).
[55] W. Zou and R. G. Larson, J. Rheol. **58**, 681 (2014).